Flow structures in subsonic-to-supersonic mixing processes using different injector geometries

Anja Wohler⋆*, Khadijeh Mohri*⋆⋆*, Christof Schulz*⋆⋆ *and Bernhard Weigand*⋆
⋆*Institut für Thermodynamik der Luft- und Raumfahrt (ITLR), Universität Stuttgart*
Pfaffenwaldring 31, 70569 Stuttgart, Germany
⋆⋆*Institut für Verbrennung und Gasdynamik (IVG), Universität Duisburg-Essen*
Lotharstr. 1, 47057 Duisburg, Germany

Abstract

Results are presented from experimental as well as numerical work that investigate the mixing behaviour in a supersonic duct flow. Four different injectors all with their trailing edges in the subsonic part of the flow and designed as wing bodies that act like a bluff body wake generator are compared. A toluene nitrogen mixture is added into the flow through the injectors and thus the flow structures behind the injector trailing edges are visualized using the laser-induced fluorescence (LIF) measurement technique. The injector flow is parallel to the duct flow and at an angle of 45° and 90° to the ambient air flow. Furthermore, one injector is designed with ramps on the top and bottom surface. Instantaneous images show that the mixing process is dominated by separated shear layers behind the injectors which roll up to vortices being shed from the blunt trailing edge. The injector flow spreads out more with increasing angle of the injector flow to the ambient air flow and the edges of the vortices are more frayed. In case of the ramp injector additional streamwise vortices are generated and thus the mixing takes place in the core region of the flow for a longer distance. Scaling properties such as the half width, the gradient of the growing wake and the virtual origin are calculated for the LIF intensity profiles as well as for the computed velocity deficit profiles. This shows that both, the half width of the LIF intensity profiles and the half width of the velocity deficit profiles, follow the $1/2$ power law scaling.

1. Introduction

In the future nanomaterials and ultrathin functional coatings of nanoparticles will play an important role in engineering applications. Nanoparticles are much smaller than the corresponding bulk material and therefore posses differing properties, e.g. electrical, optical, magnetic, chemical and mechanical characteristics. Thus they can be used in many products such as super hard materials, dirt repellent surfaces and scratchproof coatings to name a few. Consequently the production of nanoparticles is of high industrial importance. Currently flame and hot-wall synthesis are the most widely used methods for industrial production. Several studies (e.g. Schild et al. [10]) showed that a homogeneous flow field and high heating and quenching rates are the most important surrounding conditions to produce nanoparticles with narrow size distribution and low aggregation. These lead to a novel method to produce nanoparticles from gas phase precursors in a shock-wave flow reactor which is studied in the project "Gasdynamically induced nanoparticles (GiP)" supported by the Deutsche Forschungsgemeinschaft (DFG) [3]. In contrast to the conventional methods the gas mixture is instantaneously heated by a stationary shock wave of an over expanded supersonic nozzle flow. The schematic of the GiP process is shown in Fig. 1. High temperature (1300 K) and high pressure (10 bar) gas produced by a pore burner is accelerated in a first nozzle. The injectant, a nitrogen TEOS composition, is mixed in the ambient air and accelerates to supersonic flow speed. The reaction is then initiated by a shock wave at the end of the first nozzle. The temperature rise starts the chemical processes which lead to the generation and growth of nanoparticles in the reaction volume. The reaction volume is variable in its length and therefore the reaction time is adjustable. In a second convergent-divergent nozzle the flow is accelerated to supersonic speed again and thus the temperature is lowered. Finally the total enthalpy of the flow is reduced by injecting water in a quenching system.

However, a spatially and temporally homogeneous mixture of the injectant with the ambient air is required to achieve high quality particles with a narrow size distribution. Due to the high velocity and short mixing time, efficient

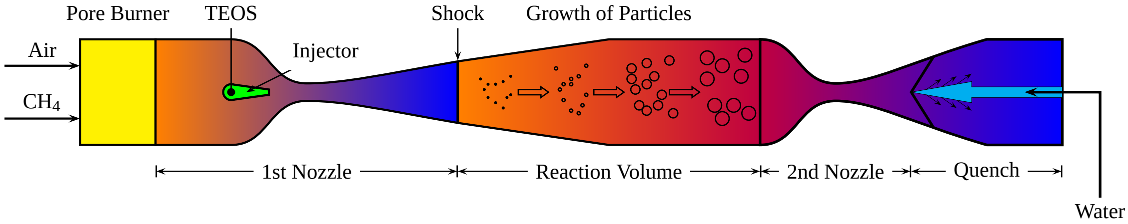

Figure 1: Schematic of the GiP process based on [5]

and rapid mixing is necessary. Hence, the mixing process was investigated from the end of the injector trailing edge to the shock train both experimentally and numerically.

However, mixing is not important in the GiP project only. Also in combustion processes, when rapid fuel and air mixing is desired, large entrainment rates of oxidizer into the injected fuel stream are aimed to be achieved. Due to the importance of these mixing processes extensive research has been done in the past. Most of the investigations dealt with incompressible wakes or with wakes in supersonic flows. Brown and Roshko [2] were the first that investigated the structure of planar mixing layers. They found that large-scale two-dimensional coherent structures play an important role in entrainment and mixing processes in incompressible shear layers. Investigations also showed that compressibility effects strongly impact the structures. Moreover, the spreading rate of the mixing layer decreases with increasing Mach number. Two decades later Gutmark et al. [6] presented a detailed review of incompressible and compressible shear flows. Recent studies from Nakagawa and Dahm [8] presented scaling properties of confined, supersonic, planar, turbulent, bluff-body wakes at different Mach numbers. Further intensive research has been done for RAMJET and SCRAMJET engines. Gerlinger et al. [4] investigated different lobed injector geometries for use in SCRAMJET engines at combustor Mach numbers around two. They found, that these geometries generate large-scale streamwise vortices and thus improve mixing. Most of these papers dealt with mixing layers in regions with a constant pressure gradient whereas in the supersonic duct used by the GiP project the wake starts in the subsonic part of the Laval nozzle and is then accelerated to supersonic flow speed. Another difference is that in most studies the jet had a higher or at least a comparable speed as the co-flow. In contrast, the velocity of the injected precursor gas flow in the present study is significantly lower than the ambient air flow speed at the injector trailing edge. To investigate the wake structure laser-induced fluorescence (LIF) imaging method using a toluene seeded nitrogen flow as a replacement for the precursor flow was applied. The fluorescence properties of toluene are well characterized and this component is therefore used for the investigation of the spatial distribution.

2. Experiments

The experiments were conducted using the supersonic test facility at the Institut für Thermodynamik der Luft- und Raumfahrt (ITLR) at the University of Stuttgart. A schematic of the facility is shown in Fig. 2. It contains a screw compressor, an air dryer, a two staged electrical heater and the optically accessible test section. The continously operating screw compressor delivers air at a maximum of 10 bar with a mass flow rate of 1.45 kg/s. The dried and compressed air can be heated up to 1500 K. The total pressure and the total temperature of the air stream were measured at the exit of the second heater with uncertainties of ±0.1 bar and ±1.0%, respectively. The mass flow rate of the air stream was measured with a vortex flow meter in combination with temperature and pressure instruments (combined maximum uncertainty less than ±9%).

2.1 Description of the flow

In the present paper an air flow through a rectangular Laval nozzle with a width of 40 mm, a total length of 800 mm and a nozzle throat height of 20 mm was observed. In all following descriptions, the x-coordinate represents the streamwise direction, the y-axis defines the spanwise direction and the z-axis is normal to the flow. The origin of the coordinate system is located in the center of the nozzle throat.

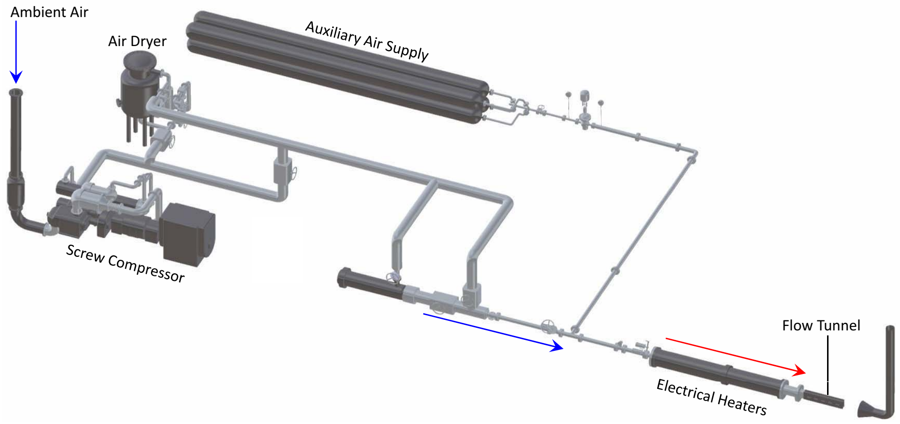

Figure 2: Schematic of the supersonic test facility at the ITLR

In all experiments the ambient air flow had a total pressure of 2 bar and a total temperature of 380 K. Thus, the Reynolds number based on the nozzle throat is about $Re \approx 578.000$ and the mass flow rate was 0.330 kg/s. The injector is mounted shortly before the nozzle throat. In this study four different injectors were tested. All were designed as a wing body with injector holes at the injector trailing edge that lies at x = -42.1 mm (see Fig. 3). Injector 1 had four injecting holes each with a diameter of 2.5 mm (see Fig. 4(a)) so that the injector flow was parallel to the ambient air flow direction. In contrast the injector flow direction in case of injector 3 and injector 4 was at an angle of 45° (see Fig. 4(c)) and 90° (see Fig. 4(d)) to the normal flow direction, respectively. Injector 2 had the same injector hole positions as injector 1 but was designed with ramps on the upper and lower surface of the trailing edge (see Fig. 4(b)).

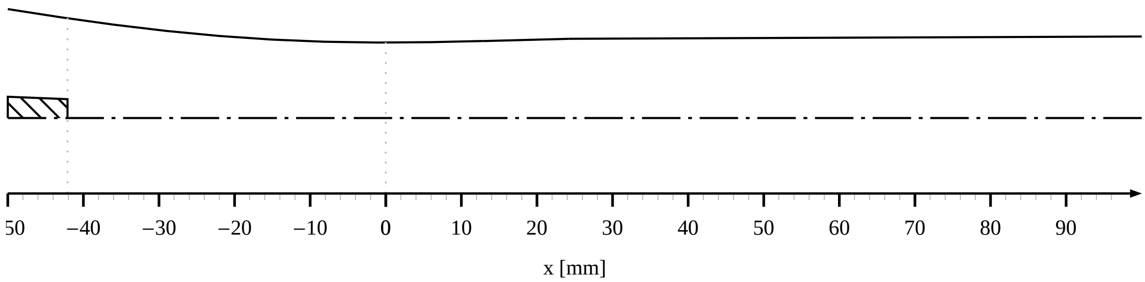

Figure 3: Duct contour till the end of the first window

A toluene seeded nitrogen flow was used as a replacement for the precursor flow and was mixed into the duct air flow using four different injector geometries. The seeded flow consisted of 0.14 g/s toluene and 0.42 g/s nitrogen. Thus, the injector massflow rate was 0.56 g/s and the injected mass flow was about $\dot{m} \approx 0.17\%$ of the ambient air flow. These mass flow amounts were kept constant throughout all experiments with all different injectors. The total temperature of the injector flow was 380 K and the total pressure was 6 bar. This corresponds to a injector flow bulk velocity of 10 m/s. Furthermore, the ambient air Mach number at the injector trailing edge is about 0.79.

2.2 Test section

The rectangular duct is made from aluminum and contains two side plates, one top plate and one bottom plate (see Fig. 5(a)). To feed a lasersheet into the duct on the top and bottom walls laser slots are integrated and follow the shape of the Laval nozzle. In addition, quartz windows are attached from both sides for optical access in order to observe the mixing from the injector trailing edge. The toluene seeded nitrogen injector flow is provided by a Controlled Evaporator Mixing (CEM) system (Bronkhorst). A controlled amount of toluene is introduced into the CEM from a reservoir. Nitrogen enters the CEM and is mixed with the evaporated toluene. In addition, nitrogen can be added to the mixture later. The gas is introduced to the injector by a heated tube to prevent the mixture from condensing. At the top wall of the duct 29 pressure tapping points are installed to measure the wall static pressure. The pressure decreases

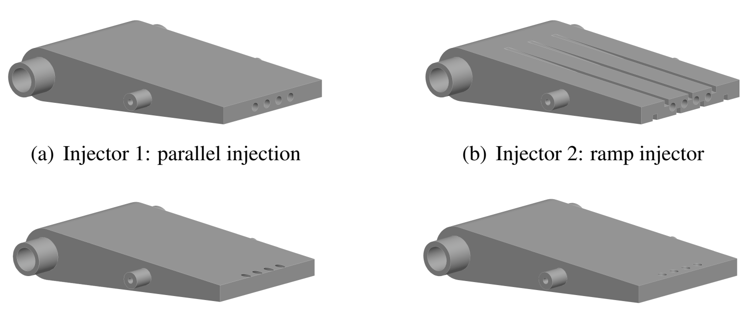

(a) Injector 1: parallel injection

(b) Injector 2: ramp injector

(c) Injector 3: 45° injection

(d) Injector 4: 90° injection

Figure 4: Different investigated injector geometries

until $x \approx 35$ mm, which indicates that the flow is accelerated to supersonic flow speed in the Laval nozzle (see Fig. 5(b)). The small increase in wall static pressure between $x \approx 35 - 120$ mm is due to the growth of the mixing layer. Further downstream the flow is accelerated by an increasing cross section. Due to overexpansion of the supersonic flow at the duct outlet a shock train decelerates the flow. The injector trailing edge ($x = -42.1mm$) and the nozzle throat ($x = 0mm$) are labeled in the diagram. Supplementary thermocouples are integrated: one in the duct flow and one in the injector flow.

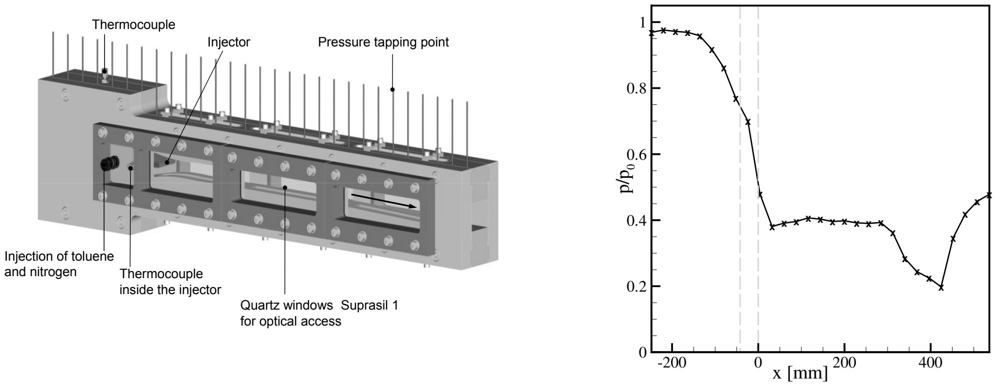

(a) Flow duct

(b) Measured wall static pressure distribution

Figure 5: Details of the supersonic duct used for mixing experiments

2.3 LIF setup

The mixing structures were visualized using the non-intrusive laser-induced fluorescence (LIF) measurement technique. A krypton fluoride excimer laser (Lambda Physik, LPX 120) with a beam at 248 nm wavelength (20 ns pulse width, broadband output) was used to excite the injector flow. The formed laser light sheet was 0.5 mm thick and 25 mm wide and passed through the duct from the top to the bottom through laser slots (see Fig. 6). Two hundred instantaneous LIF images were taken capturing the peak fluorescence signals (λ =280 ± 14 nm) at 90° to the flow. To detect the fluorescence a CCD camera with 200 ns exposure time and 8 Hz capture rate (LaVision, Imager Intense) was located perpendicular to the laser sheet plane. All optical equipment was installed on a moveable optical table that was used to shift the LIF setup along the whole duct.

3. Numerical Setup

To provide useful information about the duct flow which could not be obtained from the experiments a numerical simulation was used. A 2D structured grid was established using ICEM CFD which contains 242.552 nodes. The mesh consists of a H-grid topology in the duct and an O-grid topology around the injector to achieve a good quality

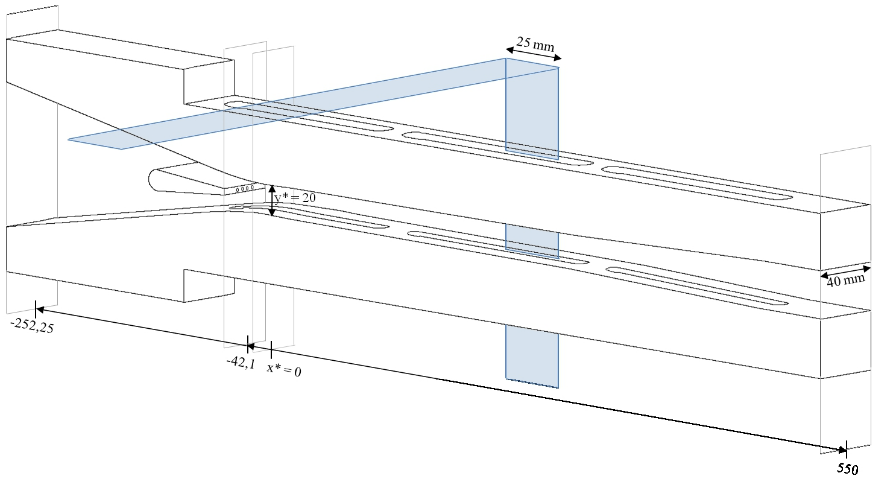

Figure 6: Schematic of the duct dimensions and the lasersheet

grid. The flow field was simulated using the commercial computational fluid dynamic (CFD) code ANSYS CFX. The unsteady Reynolds averaged Navier Stokes equations (URANS) were solved by an implicite solver with second order time and space approximation. The $k - \Omega$ shear stress transport ($k - \Omega$ SST) turbulence model developed by Menter [7] was used. Furthermore, the following boundary conditions were applied to the grid: the inlet was set to a pressure inlet with the same total pressure and total temperature as in the experiment ($p_0 = 2$ bar and $T_0 = 380$ K). At the outlet a surrounding domain was created so that the shocktrain at the end of the duct is not disturbed. At the surrounding domain the pressure was set to the measured ambient air pressure of $p_\infty = 0.96$ bar. All walls were set adiabatic. Due to the highly transient nature of the flow an unsteady computation with a single timestep of $2 \cdot 10^{-8}$ s was conducted. The duct flow without injector flow was simulated only to investigate the vortex shedding since the injector itself acts like a bluff-body wake generator. Thus, the simulation clearly shows the velocity deficit and the pressure and temperature distribution over the entire duct height.

4. Results and Discussion

From the unsteady simulation the frequency of the vortex shedding induced by the injector trailing edge is computed to be $f = 8.4 \cdot 10^{-5}$ 1/s. From this the Strouhal number related to the injector trailing edge height can be calculated, $St = 0.22$, with a free stream velocity at the injector trailing edge of $U_\infty = 270$ m/s which denotes a free stream Mach number of 0.79. This value is typical for vortex shedding behind a blunt trailing edge. Due to the slow sampling rate of the transducers the measured wall static pressure represents an averaged value. For comparison the numerical results from each timestep in one circle were averaged as well. The measured and computed averaged wall static pressure distributions are compared in Fig. 7. The circles denote the experimental data while the solid line represents the numerical results. It can be seen that there is a very good agreement between both results.

4.1 LIF images

The recorded raw LIF images must be post-processed to correct for contribution of scattered laser light that was not fully suppressed by the applied filters as well as the local variation due to inhomogeneities in the laser light sheet. For correction, background images were taken without injecting toluene into the channel. The signal distribution observed in these background measurements was then subtracted from the measured images. The images were then corrected for light sheet inhomogeneities using images that were taken without gas flow after filling the test section with a homogeneous mixture of nitrogen and toluene. These corrected LIF images provide good qualitative results showing the flow structures behind the injector trailing edges.

Instantaneous toluene LIF images observed in the first duct window using the explained injector geometries are shown in Fig. 8. In case of injectors 1, 3 and 4 (Fig. 8(a), 8(c) and 8(d)) it can be seen clearly that the mixing process is dominated by separated shear layers behind the injector which roll up to vortices being shed from the blunt injector

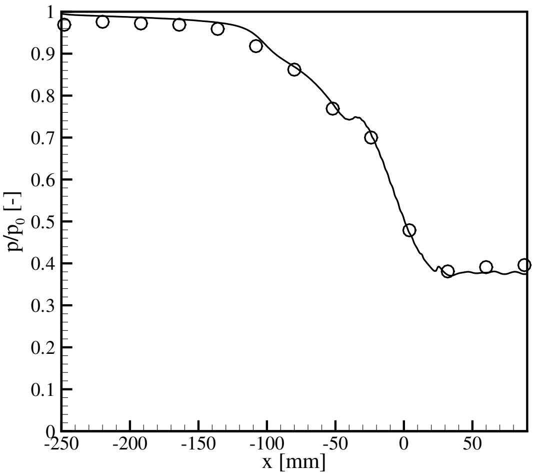

Figure 7: Averaged wall static pressure distribution, both experimental (circles) and numerical values (solid line)

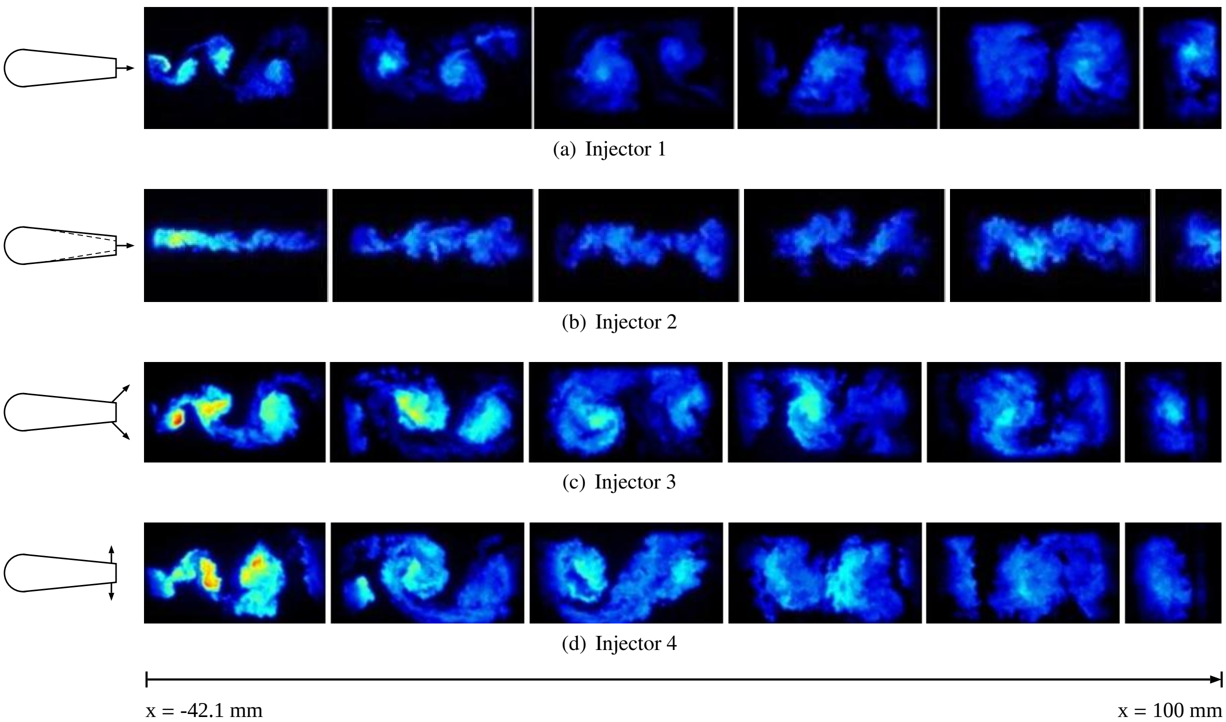

Figure 8: Instantaneous toluene LIF images of the first duct window using different injector geometries

trailing edge. The primary length scale of the large turbulent structures is determined by the thickness of the injector's trailing edge. The images show the typical counter rotating vortical structure of the wake and the wave pattern between two neighboring vortices. Due to the fact that the injector flow was at an angle of 45° and 90° in case of injectors 3 and 4 respectively the visible vortex structures are larger, the injector flow is spread out more and the edges of the vortices are frayed. Consequently, the injector flow reached the test section height at a position more upstream compared to injector 1. In contrast, additional streamwise vortices with strong axial vorticity were generated in case of injector 2 (see Fig. 8(b)). Thus, the mixing of the toluene nitrogen injector flow with the ambient air takes place in the core region of the flow for a longer distance.

4.2 Averaged LIF intensity

The instantaneous LIF images presented in the previous section showed the vortical structures behind the injector trailing edge in detail. To get more information about the growth rate of the wake averaged LIF images are needed. For this all 200 instantaneous images were averaged and also corrected for background signal and lasersheet energy variations. LIF intensity profiles are plotted from the averaged images in Fig. 9 for some positions downstream of the injector trailing edge obtained for injector 1. All intensity profiles were normalized to the maximum intensity directly at the injector trailing edge.

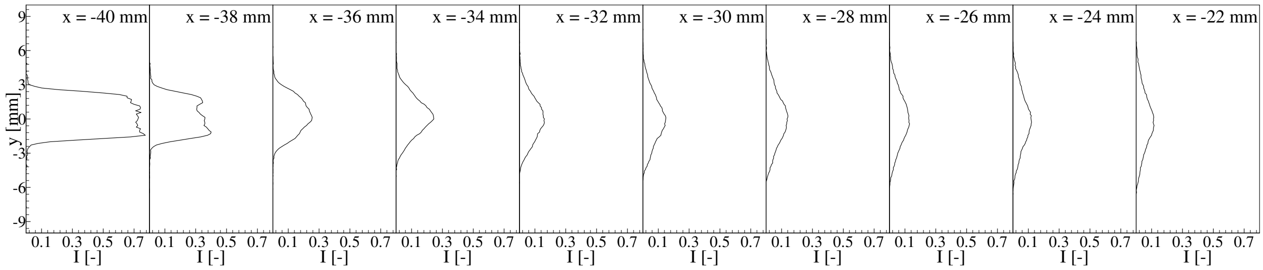

Figure 9: LIF intensity profiles obtained from injector 1

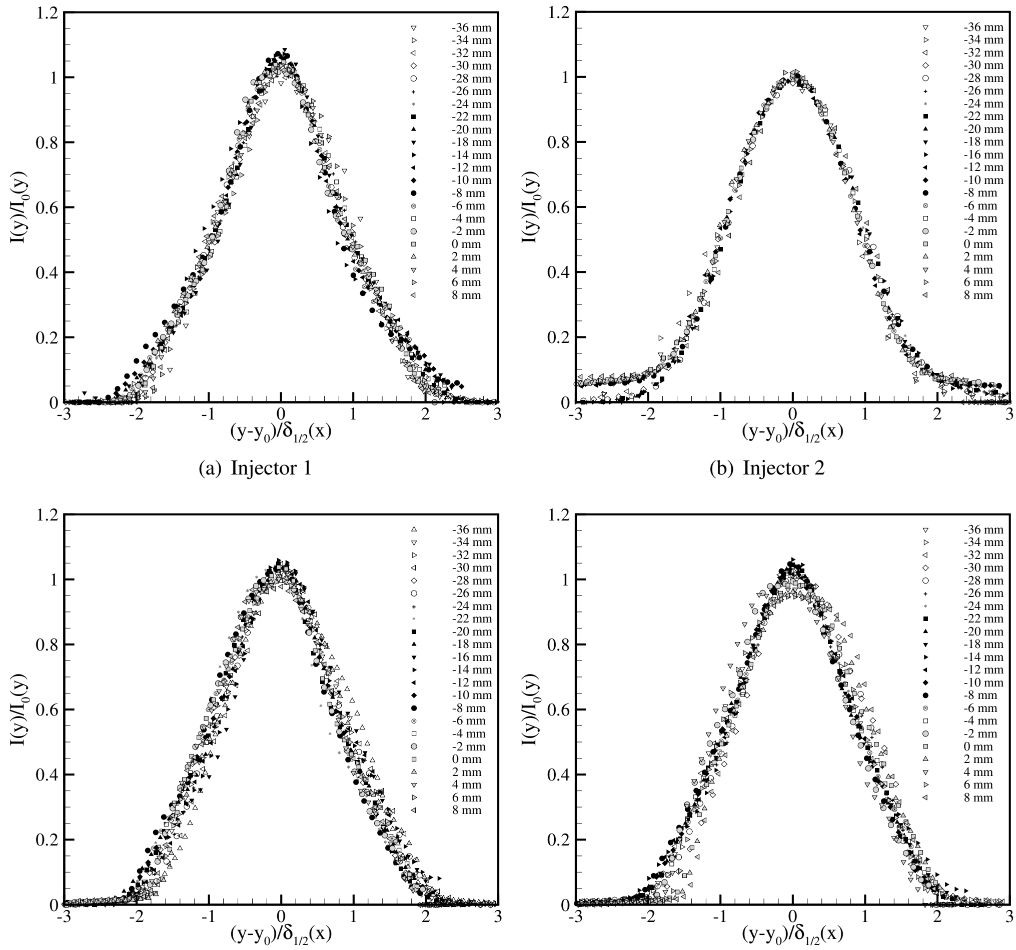

(a) Injector 1

(b) Injector 2

(c) Injector 3

(d) Injector 4

Figure 10: Similarity of the toluene intensity profiles at different downstream locations for all different injectors

It can be clearly seen that the maximum intensity in the middle of the duct decreases and the toluene spreads out with downstream location. To quantify the visual thickness of the wake a Gaussian fit was applied to all intensity profiles over the central portion of the flow in steps of 2 mm up to 10 trailing edge thicknesses downstream of the trailing edge. From this fitting the local centerline position $y_0(x)$, the local maximum intensity $I_0(x)$ and the local visual width $\delta_{1/2}(x)$ of each downstream intensity profile were obtained. Figure 10 shows all local mean intensity profiles obtained from the averaged LIF images. All profiles are normalized by the local maximum value $I_0(x)$. In the lateral direction the difference between y and the maximum location y_0 normalized by the local half-width $\delta_{1/2}(x)$ is plotted. The figures show that the profiles are nearly self similar for all four injectors.

From the LIF intensity profiles shown in Fig. 9 and the Gaussian fit the local visual width $\delta_{1/2}(x)$ of each downstream intensity profile was calculated. Various studies showed that the growth rate of the wake is directly proportional to the mean root square of the distance to the injector trailing edge ($\delta_{1/2} \sim x^{1/2}$). Figure 11(a) shows the squared growth rate at different axial positions for all different injectors. In accordance to the theory the symbols show a constant growth rate with increasing distance from the injector. To show this behavior more clearly the method of least squares was applied to the experimental results and the best-fit line was plotted for each injector in Fig. 11(b).

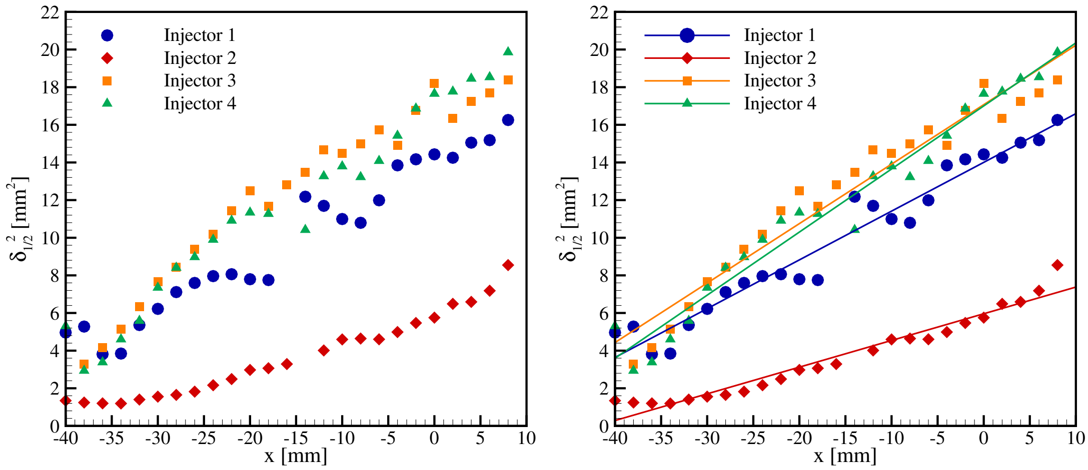

(a) Visual half width of the wake

(b) Best fit lines calculated with the method of least squares

Figure 11: Half width of the averaged LIF intensity profiles

Apparently the injector with the lowest growing rate is injector 2. Due to the ramps that create additional streamwise vortices the flow is held in the center of the duct for a longer distance and does not spread out as much as in case of injectors 1, 3 and 4. This behavior could already be seen in the instantaneous images clearly (cf. Fig. 8(b)). In contrast, the difference in the growing rate of the first three injectors could not be seen that obviously in the instantaneous LIF images. Figure 11(b) shows that the growth rate for all these three injectors is much larger than for injector 2. Furthermore, the growth rate increases with increasing injection angle. The largest growth rate is seen for injector 4. This is in accordance with the fact that the toluene nitrogen mixture is fed into the ambient air at an angle of 90° with this injector. Hence, as expected the growing rate of the wake for injector 3 is smaller than for injector 4 but still larger than in case of injector 1. From the best-fit line calculated with the method of least squares the origin of the wake x_0 and the gradient $\Delta = \sqrt{\delta_{1/2}(x)^2/(x - x_0)}$ of the growing rate were calculated and the results are summarized in Table 1 for all four injectors.

	angle of injection	x_0 [mm]	Δ [mm]
injector 1	0°	-54.05	0.26
injector 2	0°, ramp injector	-42.01	0.14
injector 3	45°	-54.03	0.32
injector 4	90°	-50.73	0.34

Table 1: Origin and gradient of the growing wake obtained from the LIF images

4.3 Velocity deficit

The computed and averaged velocity deficit profiles are plotted at different axial positions starting shortly behind the injector trailing edge in Fig. 12. At the injector trailing edge the profile is characterized by a very large velocity deficit with a narrow spreading rate. Further downstream the velocity deficit becomes smaller and the width of the wake becomes larger. The velocity deficit can be found up to 10 trailing edge thicknesses downstream of the trailing edge. Further downstream, one can see that the bluff body no longer influences the averaged velocity profile. From these profiles the half width of the velocity deficit was calculated at different axial positions and is shown in Fig. 13. The diagram shows that the velocity deficit wake grows faster than the visual width obtained with the averaged LIF images. Furthermore, the same scaling properties than for the visual wake were calculated. The origin of the velocity wake results in $x_0 = -49.07$ and the gradient of the growing wake was calculated to be $\Delta = 0.54mm$.

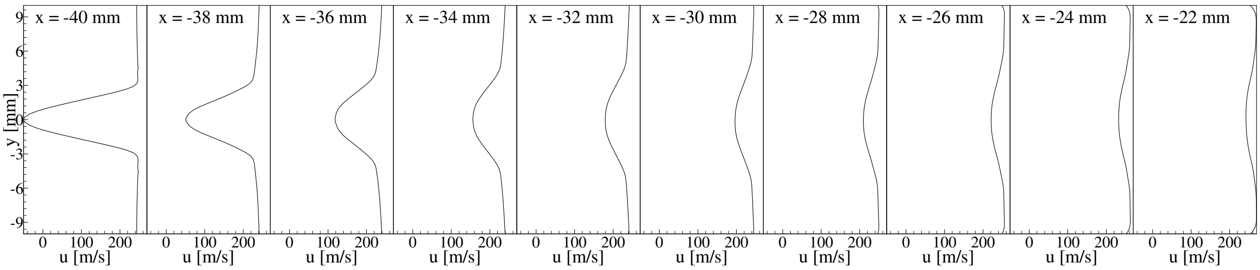

Figure 12: Computed velocity profiles without injector flow

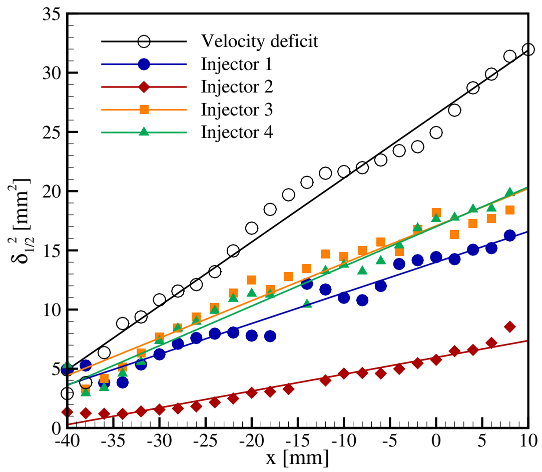

Figure 13: Half width of the velocity deficit created by the bluff body injector

5. Conclusions and future work

The mixing behavior of four different injectors, all with their trailing edges in the subsonic region of the flow were tested in a supersonic duct with diverging walls using the LIF measurement technique. The instantaneous images show qualitative differences in the mixing behavior and from the averaged images scaling properties such as the half width, the gradient of the growing wake and the virtual origin were calculated. In addition the dimensionless intensity profiles were plotted at different axial locations and they show a nearly self similar behavior. Furthermore, results of an unsteady numerical simulation were used to plot the growing rate of the velocity deficit wake. It was shown that both, the half width of the LIF intensity profiles and the half width of the velocity deficit profiles follow the $1/2$ power law scaling. In further work, the LIF images will be corrected for quenching effects due to varying flow properties, e.g. temperature and oxygen partial pressure along the duct. Furthermore, the numerical simulations will include the toluene nitrogen injector flow for comparison it with the LIF data. In further experimental work injectors with their trailing edges in the supersonic part of the diverging duct will be investigated.

6. Acknowledgements

The authors gratefully acknowledge funding by the Deutsche Forschungsgemeinschaft, DFG.

References

[1] Anderson Jr., J. D. 1990. Modern Comperssible Flow - With historical perspective. *McGraw-Hill Publishing Company*. Singapore. Second Edition.

[2] Brown, G. L. and A. Roshko. 1974. On density effects and large structure in turbulent mixing layers. *Journal of Fluid Mechanics*. 64: 775–816.

[3] Dannehl M., A. Maisels, W. Leibold, H. Olivier, A. Grzona, A. Weiß, A. Gülhan, T. Gawehn, G. H. Schnerr, N. Al-Hasan, A. Abdali, M.Y. Luong, H. Wiggers, C. Schulz, B. Weigand, J. Chun, W. Schröder, M. Meinke, T. Winnemöller, H. Nirschl, V. Goertz, K. Schaber and T. Rakel. 2007. Nanoparticle Synthesis by Gas-dynamically Induced Heating and Quenching. *European Aerosol Conference 2007*.

[4] Gerlinger, P., P. Kasal, F. Schneider, J. von Wolfersdorf, B. Weigand and M. Aigner. 2005. Experimental and Numerical Investigation of Lobed Strut Injectors for Supersonic Combustion. *John Wiley & Sons*. Chapter 5.5: 365–382.

[5] Grzona, A., A. Weiß, H. Olivier, T. Gawehn, A. Gülhan, N. Al-Hasan, G.H. Schnerr, A. Abdali, M. Luong, H. Wiggers, C. Schulz, J. Chun, B. Weigand, T. Winnemöller, W. Schröder, T. Rakel, K. Schaber, V. Goertz, H. Nirschl, A. Maisels, W. Leibold, and M. Dannehl. 2007. Gas-phase synthesis of non-agglomerated nanoparticles by fast gasdynamic heating and cooling. *ISSW*. Göttingen.

[6] Gutmark, E. J., K. C. Schadow and K. H. Yu. 1995. Mixing Enhancement in Supersonic Free Shear Flows. *Annual Review of Fluid Mechanics*. 27: 375–417.

[7] Menter, F. R. 1994. Two-Equation Eddy-Viscosity Turbulence Models for Engineering Applications. *AIAA Journal*. 32: 1598–1605

[8] Nakagawa, M. and W. J. A. Dahm. 2006. Scaling Properties and Wave Interactions in Confined Supersonic Turbulent Bluff-Body Wakes. *AIAA Journal*. 44: 1299–1309.

[9] Papamoschou, D. and A. Roshko. 1988. The compressible turbulent shear layer: an experimental study. *Journal of Fluid Mechanics*. 197: 453–477.

[10] Schild A., Gutsch A., Mühlenweg H. and S. E. Pratsinis. 1999. Simulation of nanoparticle production in premixed aerosol flow reactors by interfacing fluid mechanics and particle dynamics. *Journal of Nanoparticle Research*. 1: 305–315.